Numerical Simulation in Applied Geophysics. From the Mesoscale to the Macroscale

Juan E. Santos ,[†] Patricia M. Gauzellino [*], Gabriela B. Savioli[**] and Robiel Martinez Corredor[†,†]

[†] CONICET, Instituto del Gas y del Petróleo, Facultad de Ingeniería UBA, UNLP and Department of Mathematics, Purdue University.

[*] Facultad de Cs. Astr. y Geofísicas, UNLP

[**] Instituto del Gas y del Petróleo, Facultad de Ingeniería UBA

[†,†] Facultad de Ingeniería, UNLP

Introduction. I

- **Seismic wave propagation** is a common technique used in hydrocarbon exploration geophysics, mining and reservoir characterization and production.

- Local variations in the fluid and solid matrix properties, fine layering, fractures and craks at the mesoscale (on the order of centimeters) are common in the earth's crust and induce attenuation, dispersion and anisotropy of the seismic waves observed at the macroscale.

- These effects are caused by equilibration of wave-induced fluid pressure gradients via a **slow-wave diffusion** process.

Introduction. II

- Due to the **extremely fine meshes** needed to properly represent these type of mesoscopic-scale heterogeneities, numerical simulations are very expensive or even not feasible.

- **Suggested approach:** Use a **numerical upscaling procedure** to determine the complex and frequency dependent stiffness at the macroscale of an equivalent viscoelastic medium including the mesoscopic-scale effects.

- To determine the **complex stiffness** coefficients of the **equivalent medium**, we solve a set of boundary value problems (BVP's) for the wave equation of motion in the frequency-domain using the finite-element method (FEM).

Introduction. III

- The BVP's represent **harmonic tests** at a finite number of frequencies on a representative sample of the material.

- **Numerical rock physics** offer an alternative to laboratory measurements.

- Numerical experiments are inexpensive and informative since the physical process of wave propagation can be inspected during the experiment.

- Moreover, they are repeatable, essentially free from experimental errors, and may easily be run using alternative models of the rock and fluid properties.

The Mesoscale. Anisotropic poroelasticity. I

- To model mesoscopic effects we need a suitable differential model.

- As example, we will describe the numerical experiments on a representative sample of fluid-saturated sample having a dense set of horizontal fractures modeled as very thin and compliant layers.

- A dense set of horizontal fractures in a fluid-saturated poroelastic medium behaves as a   viscoelastic transversely isotropic (VTI) medium when the average fracture distance is much smaller than the predominant wavelength of the traveling waves.

- This leads to frequency and angular variations of velocity and attenuation of seismic waves.

- For fluid-saturated poroelastic media (Biot's media), White et al. (1975) were the first to introduce the mesoscopic-loss mechanism in the framework of Biot's theory.

- For fine layered poroelastic materials, the theories of Gelinsky and Shapiro (GPY, **62**, 1997) and Krzikalla and Müller (GPY, **76**, 2011) allow to obtain the five complex and frequency-dependent stiffnesses of the equivalent VTI medium.

- To test the model and provide a more general modeling tool, we present a numerical upscaling procedure to obtain the complex stiffnesses of the effective VTI medium.

- We employ the Finite Element Method (FEM) to solve Biot's equation of motion in the space-frequency domain with boundary conditions representing compressibility and shear harmonic experiments.

- The methodology is applied to saturated isotropic poroelastic samples having a dense set of horizontal fractures.

- The samples contained mesoscopic-scale heterogeneities due to patchy brine-CO_2 saturation and fractal porosity and consequently, fractal permeability and frame properties.

Let us consider isotropic fluid-saturated poroelastic layers.

$\mathbf{u}^s(\mathbf{x}), \mathbf{u}^f(\mathbf{x})$: **time Fourier transform of the displacement vector of the solid and fluid relative to the solid frame, respectively.**

$$\mathbf{u} = (\mathbf{u}^s, \mathbf{u}^f)$$

$\sigma_{kl}(u), \mathbf{p}_f(u)$**: Fourier transform of the total stress and the fluid pressure, respectively**

On each plane layer n in a sequence of N layers, the frequency-domain stress-strain relations are

$$\sigma_{kl}(u) = 2\mu\,\varepsilon_{kl}(u^s) + \delta_{kl}\left(\lambda_G\,\nabla \cdot u^s + \alpha M \nabla \cdot u^f\right),$$

$$\mathbf{p}_f(u) = -\alpha M \nabla \cdot u^s - M \nabla \cdot u^f.$$

Biot's equations in the diffusive range:

$$\nabla \cdot \sigma(u) = 0,$$

$$i\omega \frac{\eta}{\kappa} u^f(x, \omega) + \nabla p_f(u) = 0,$$

$\omega = 2\pi f$: **angular frequency**

η: **fluid viscosity** κ: **frame permeability**

$\tau_{\mathbf{ij}}$: **stress tensor of the equivalent VTI medium**

For a closed system($\nabla \cdot u^f = 0$), the corresponding stress-strain

relations, stated in the space-frequency domain, are

$$\tau_{11}(u) = p_{11}\,\epsilon_{11}(u^s) + p_{12}\,\epsilon_{22}(u^s) + p_{13}\,\epsilon_{33}(u^s),$$

$$\tau_{22}(u) = p_{12}\,\epsilon_{11}(u^s) + p_{11}\,\epsilon_{22}(u^s) + p_{13}\,\epsilon_{33}(u^s),$$

$$\tau_{33}(u) = p_{13}\,\epsilon_{11}(u^s) + p_{13}\,\epsilon_{22}(u^s) + p_{33}\,\epsilon_{33}(u^s),$$

$$\tau_{23}(u) = 2\,p_{55}\,\epsilon_{23}(u^s),$$

$$\tau_{13}(u) = 2\,p_{55}\,\epsilon_{13}(u^s),$$

$$\tau_{12}(u) = 2\,p_{66}\,\epsilon_{12}(u^s).$$

This approach provides the complex velocities of the fast modes and

takes into account interlayer flow effects.

To determine the complex stiffness we solve Biot's equation in the 2D case on a reference square $\Omega = (0, L)^2$ with boundary Γ in the (x_1, x_3)-plane. Set $\Gamma = \Gamma^L \cup \Gamma^B \cup \Gamma^R \cup \Gamma^T$, where

$$\Gamma^L = \{(x_1, x_3) \in \Gamma : x_1 = 0\}, \quad \Gamma^R = \{(x_1, x_3) \in \Gamma : x_1 = L\},$$

$$\Gamma^B = \{(x_1, x_3) \in \Gamma : x_3 = 0\}, \quad \Gamma^T = \{(x_1, x_3) \in \Gamma : x_3 = L\}.$$

The sample is subjected to harmonic compressibility and shear tests described by the following sets of boundary conditions.

$p_{33(\omega)}$**:**

$$\sigma(u)\nu \cdot \nu = -\Delta P, \quad (x_1, x_3) \in \Gamma^T,$$

$$\sigma(u)\nu \cdot \chi = 0, \quad (x_1, x_3) \in \Gamma^T \cup \Gamma^L \cup \Gamma^R,$$

$$u^s \cdot \nu = 0, \quad (x_1, x_3) \in \Gamma^L \cup \Gamma^R,$$

$$u^s = 0, \quad (x_1, x_3) \in \Gamma^B, \quad u^f \cdot \nu = 0, \quad (x_1, x_3) \in \Gamma.$$

ν**: the unit outer normal on Γ**

χ**: a unit tangent on Γ so that $\{\nu, \chi\}$ is an orthonormal system on Γ.**
Denote by V the original volume of the sample and by $\Delta V(\omega)$ its (complex) oscillatory volume change.

In the quasistatic case

$$\frac{\Delta V(\omega)}{V} = -\frac{\Delta P}{p_{33}(\omega)},$$

Then after computing the average $u_3^{s,T}(\omega)$ of the vertical displacements on Γ^T, we approximate

$$\Delta V(\omega) \approx L u_3^{s,T}(\omega)$$

which enable us to compute $p_{33}(\omega)$

To determine $p_{11}(\omega)$ we solve an identical boundary value problem than for p_{33} but for a 90° rotated sample.

$p_{55}(\omega)$: **the boundary conditions are**

$$-\sigma(u)\nu = g, \quad (x_1, x_3) \in \Gamma^T \cup \Gamma^L \cup \Gamma^R,$$

$$u^s = 0, \quad (x_1, x_3) \in \Gamma^B,$$

$$u^f \cdot \nu = 0, \quad (x_1, x_3) \in \Gamma,$$

where

$$g = \begin{cases} (0, \Delta G), & (x_1, x_3) \in \Gamma^L, \\ (0, -\Delta G), & (x_1, x_3) \in \Gamma^R, \\ (-\Delta G, 0), & (x_1, x_3) \in \Gamma^T. \end{cases}$$

The change in shape suffered by the sample is

$$\tan[\theta(\omega)] = \frac{\Delta G}{p_{55}(\omega)}. \tag{1}$$

$\theta(\omega)$: **the angle between the original positions of the lateral boundaries and the location after applying the shear stresses.**

Since

$\tan[\theta(\omega)] \approx u_1^{s,T}(\omega)/L$, **where** $u_1^{s,T}(\omega)$ **is the average horizontal displacement at** Γ^T, $p_{55}(\omega)$ **can be determined from**

to determine $p_{66}(\omega)$ **(shear waves traveling in the** (x_1, x_2)**-plane), we rotate the layered sample** 90° **and apply the shear test as indicated for** $p_{55}(\omega)$**.**

$p_{13}(\omega)$: **the boundary conditions are**

$$\sigma(u)\nu \cdot \nu = -\Delta P, \quad (x_1, x_3) \in \Gamma^R \cup \Gamma^T,$$

$$\sigma(u)\nu \cdot \chi = 0, \quad (x_1, x_3) \in \Gamma,$$

$$u^s \cdot \nu = 0, \quad (x_1, x_3) \in \Gamma^L \cup \Gamma^B, \quad u^f \cdot \nu = 0, \quad (x_1, x_3) \in \Gamma.$$

In this experiment $\epsilon_{22} = \nabla \cdot u^f = 0$, **so that**

$$\tau_{11} = p_{11}\epsilon_{11} + p_{13}\epsilon_{33}, \quad \tau_{33} = p_{13}\epsilon_{11} + p_{33}\epsilon_{33}, \tag{2}$$

$\epsilon_{11}, \epsilon_{33}$: **the strain components at the right lateral side and top side of the sample, respectively. Then,**

$$p_{13}(\omega) = \left(p_{11}\epsilon_{11} - p_{33}\epsilon_{33}\right) / \left(\epsilon_{11} - \epsilon_{33}\right).$$
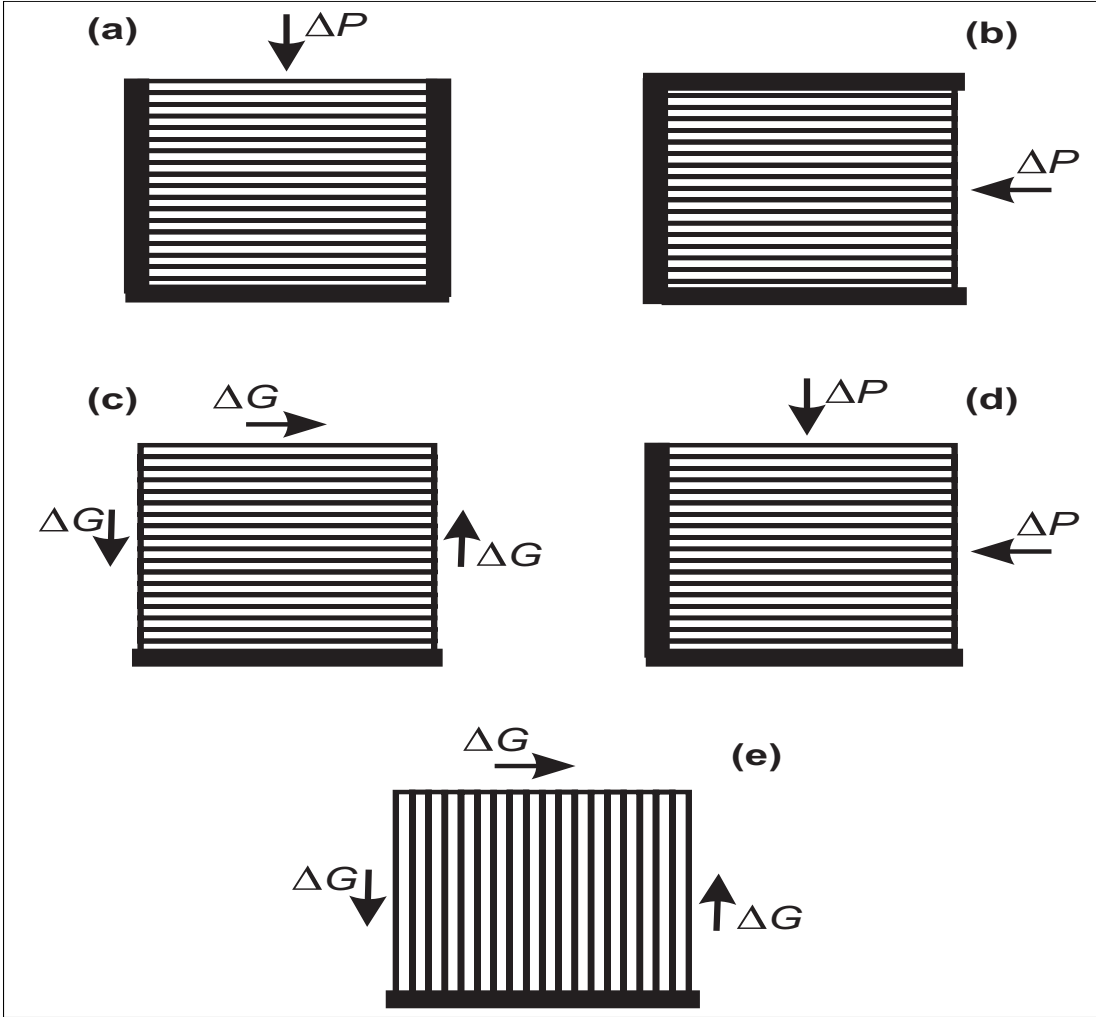
a): p_{33}, b): p_{11}, c): p_{55}, d): p_{13} e): p_{66}

A set of numerical examples consider the following cases for a square poroelastic sample of 160 cm side length and 10 periods of 1 cm fracture, 15 cm background:

- **Case 1: A brine-saturated sample with fractures.**

- **Case 2: A brine-CO_2 patchy saturated sample without fractures.**

- **Case 3: A brine-CO_2 patchy saturated sample with fractures.**

- **Case 4: A brine saturated sample with a fractal frame and fractures.**

The discrete boundary value problems to determine the complex stiffnesses $p_{IJ}(\omega)$ were solved for 30 frequencies using a public domain sparse matrix solver package.

Using relations not included for brevity, the $p_{IJ}(\omega)$'s determine in turn the energy velocities and dissipation coefficients shown in the next figures.

qP Waves

Legend:
- 1. Brine saturated medium with fractures
- 2. Patchy saturated medium without fractures
- 3. Patchy saturated medium with fractures
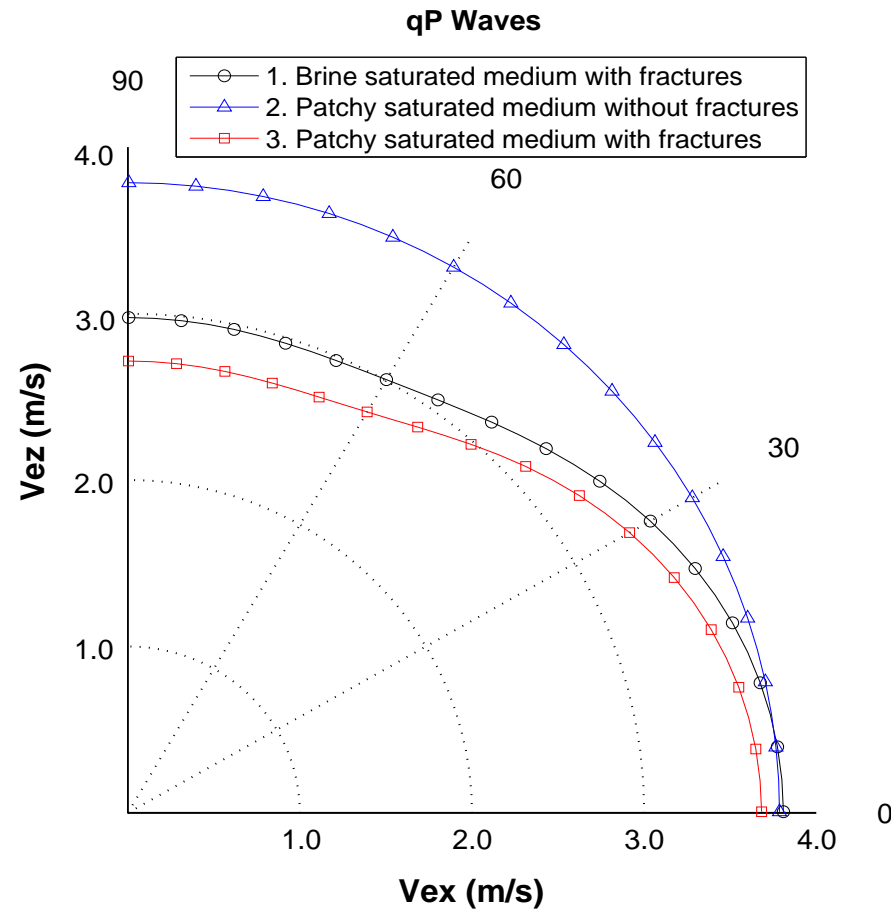
Velocity anisotropy caused by the fractures in cases 1 and 3 is enhanced for the case of patchy saturation, with lower velocities when patches are present. The velocity behaves isotropically in case 2.

qP Waves

Legend:
- 1. Brine saturated medium with fractures
- 2. Patchy saturated medium without fractures
- 3. Patchy saturated medium with fractures

Axis labels: $1000/Q$ (Z) (vertical), $1000/Q$ (X) (horizontal)
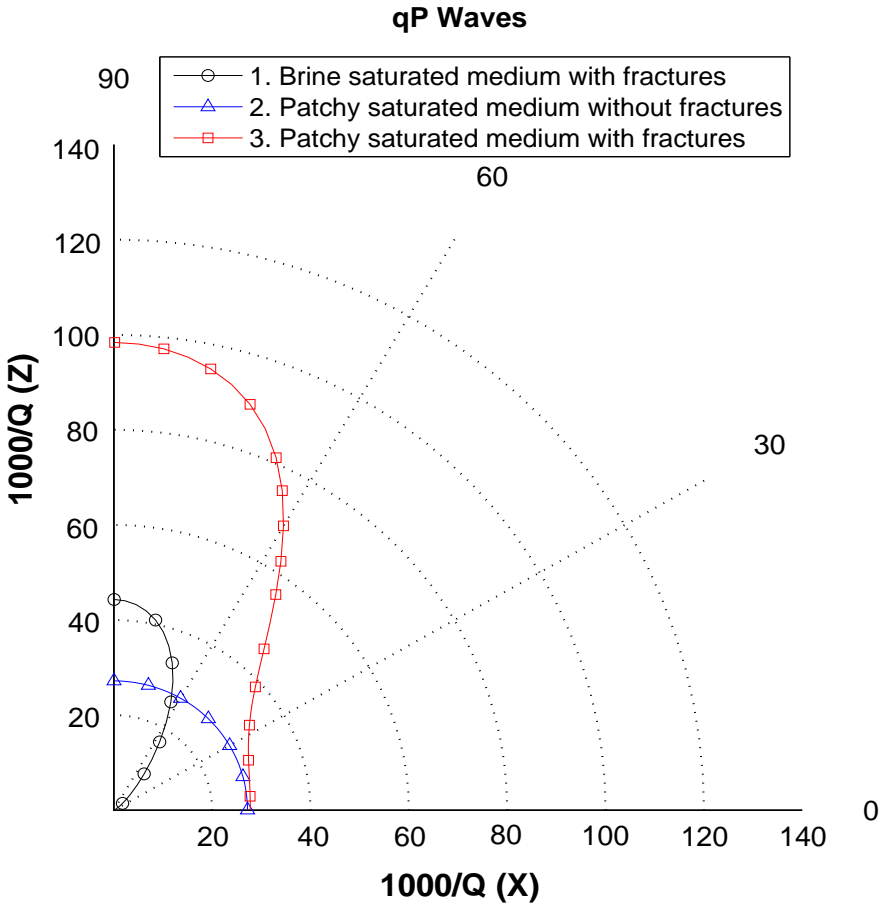
Fractures induce strong Q anisotropy for angles normal to the fracture plane, enhanced by patchy saturation.
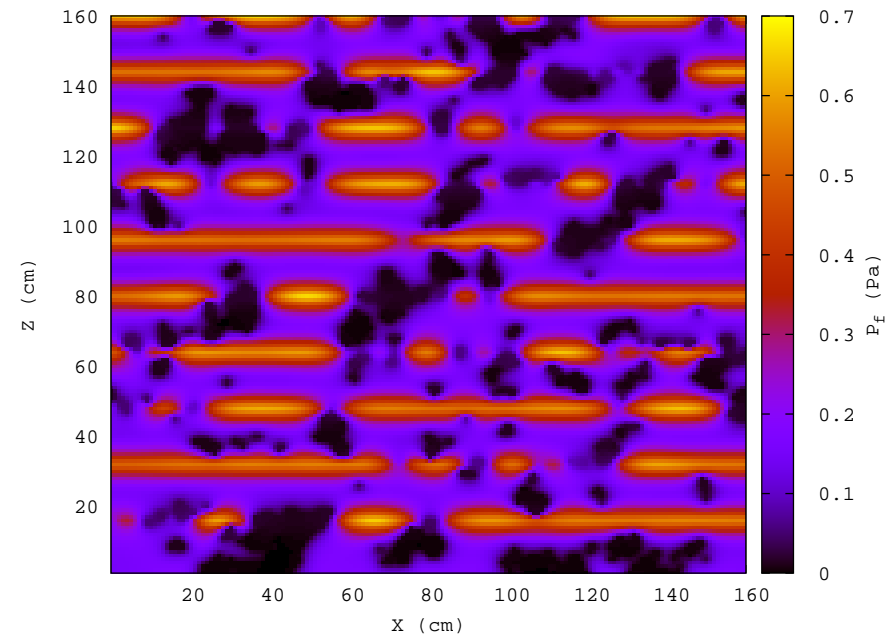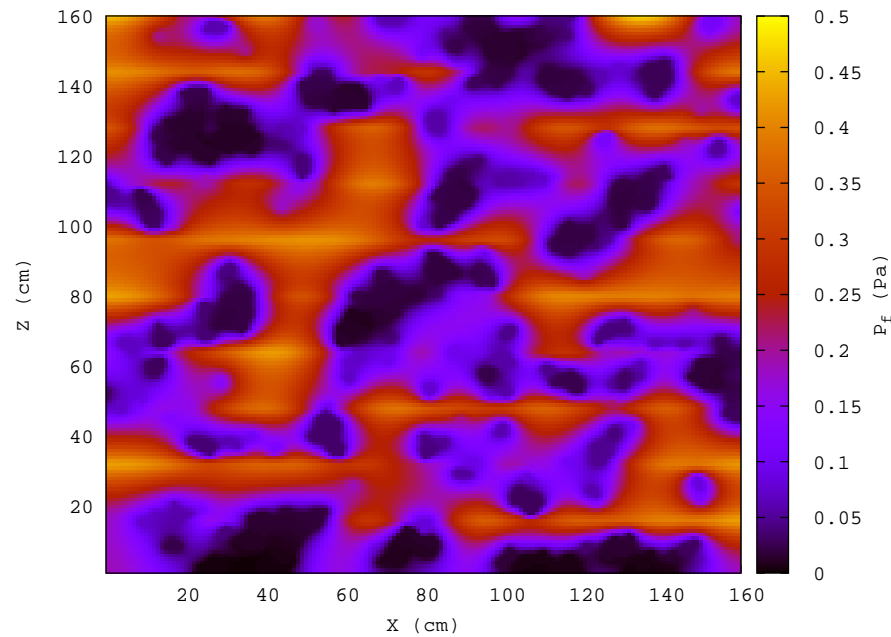
Compression is normal to the fracture plane. Attenuation is stronger at 300 Hz.
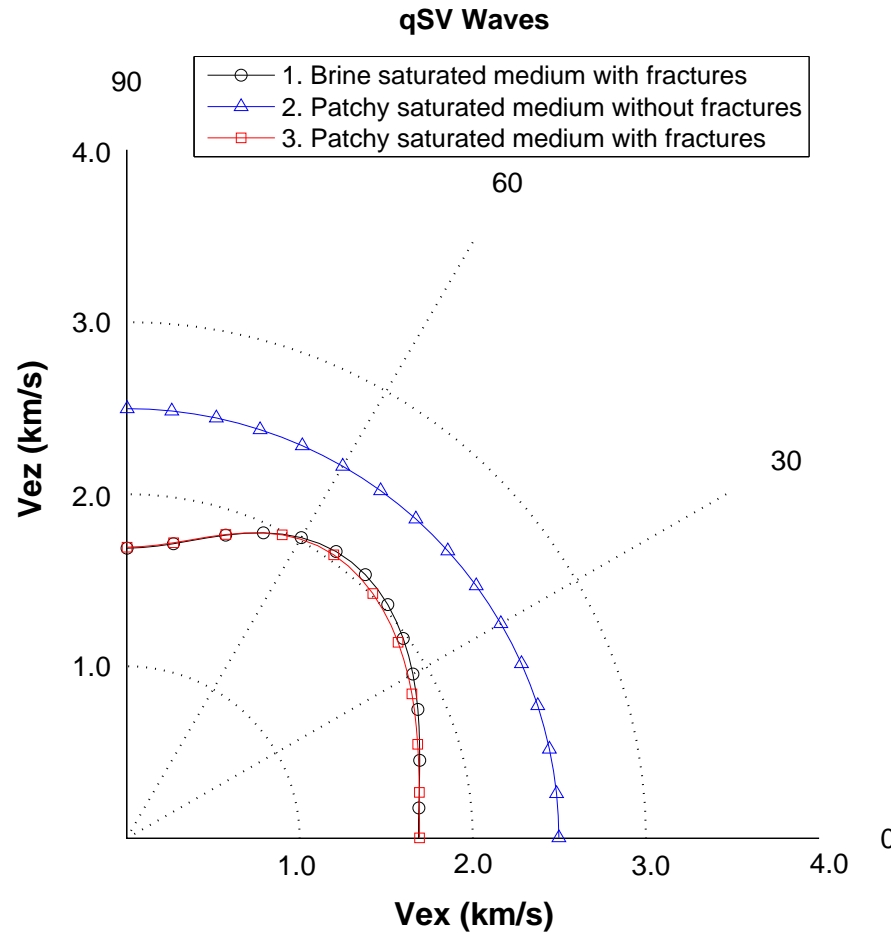
Velocity anisotropy is induced by fractures (cases 1 and 3). Patchy saturation does not affect the anisotropic behavior of the qSV velocities. Case 2 shows isotropic velocity, with higher velocity values than for the fractured cases

qSV Waves

1. Brine saturated medium with fractures
2. Patchy saturated medium without fractures
3. Patchy saturated medium with fractures
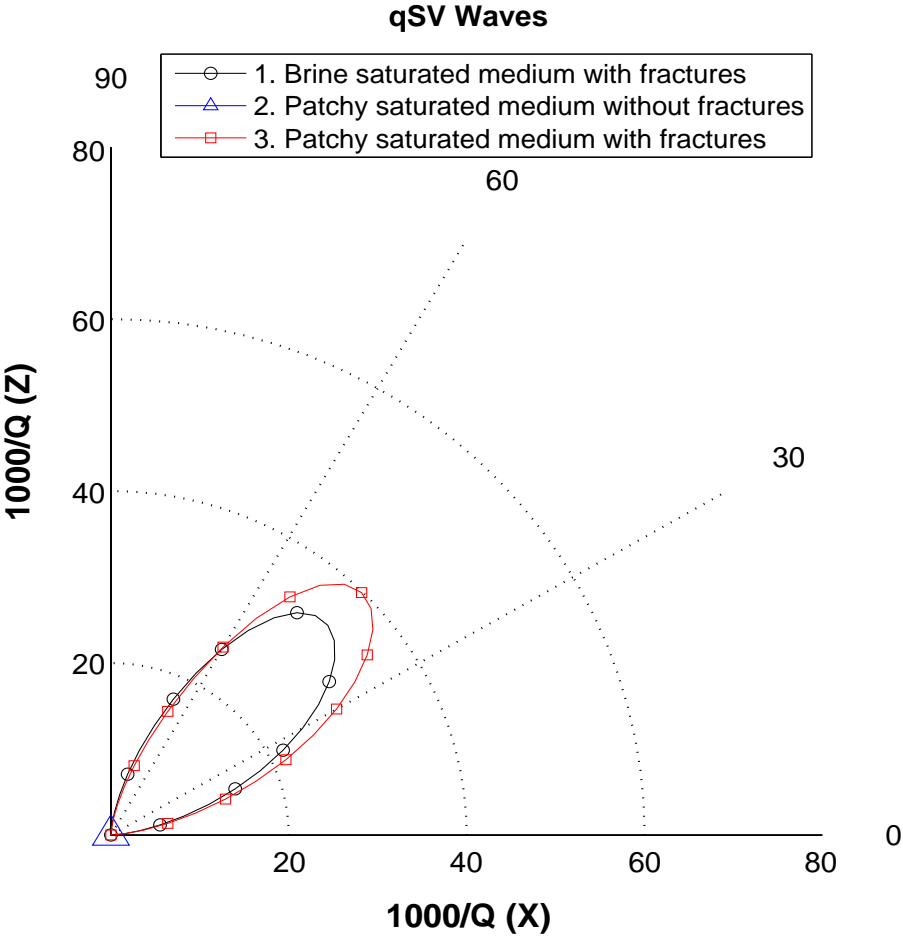
qSV anisotropy is strong for angles between 30 and 60 degrees. The lossless case 2 is

represented by a triangle at the origin
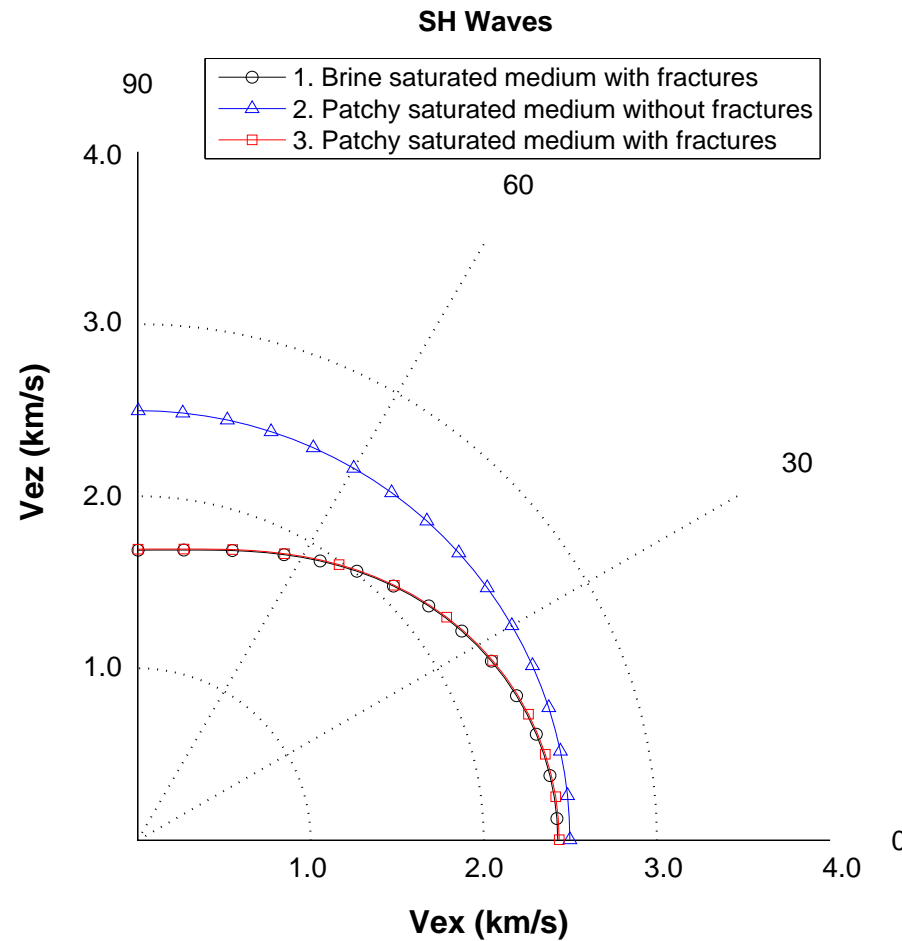
SH velocity anisotropy is observed to be induced by fractures. Cases 1 and 3 are almost indistinguishable. Velocity for case 2 is isotropic. SH waves are lossles, since p_{55} and p_{66} are real.
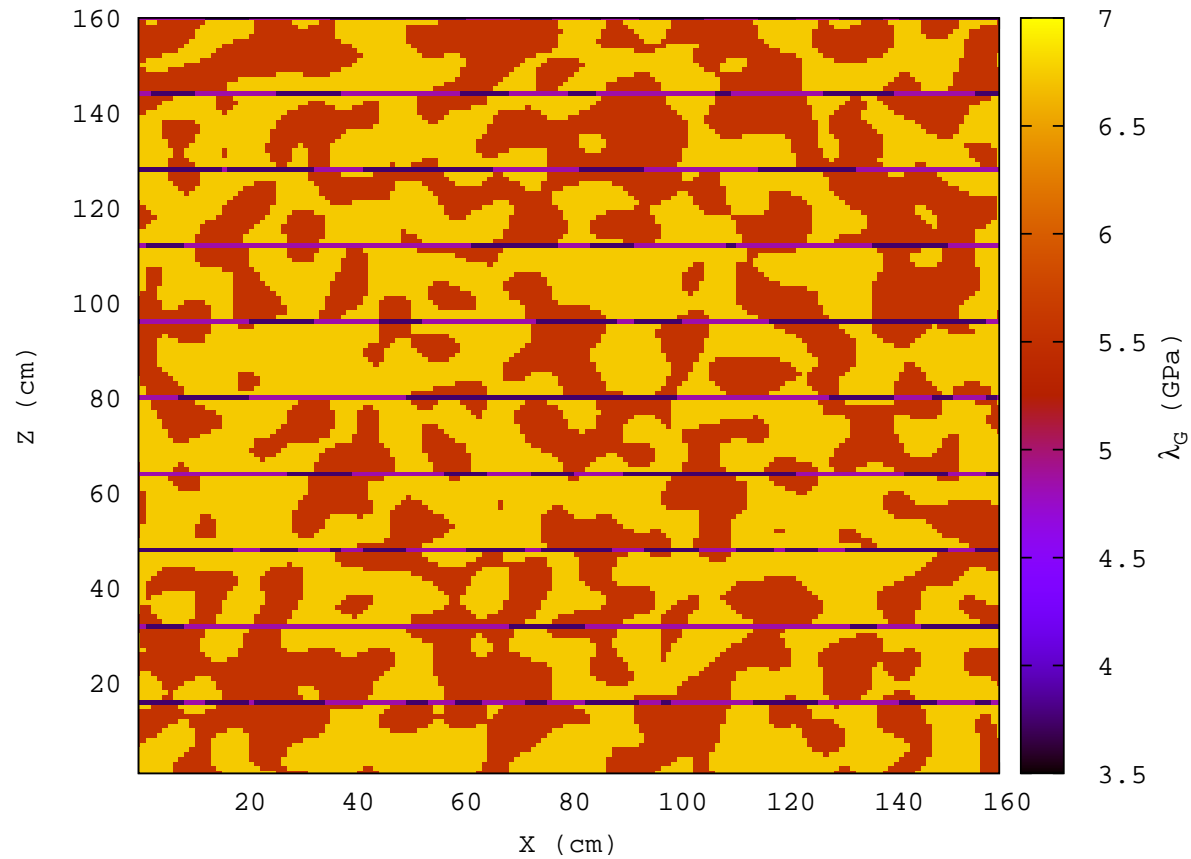
$\log \kappa(x,z) = \langle \log \kappa \rangle + f(x,z)$, $f(x,z)$: fractal representing the spatial fluctuation of the permeability field $\kappa(x,z)$.
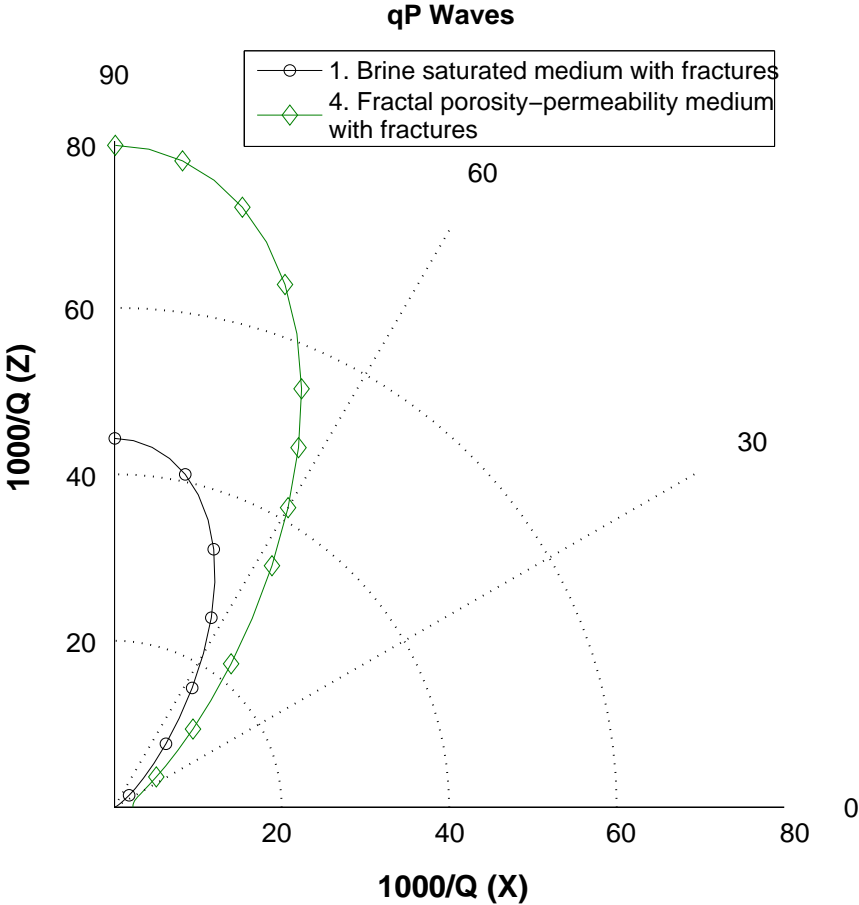
Note the increase in Q anisotropy for qP waves for angles normal to the fracture plane.

qSV Waves
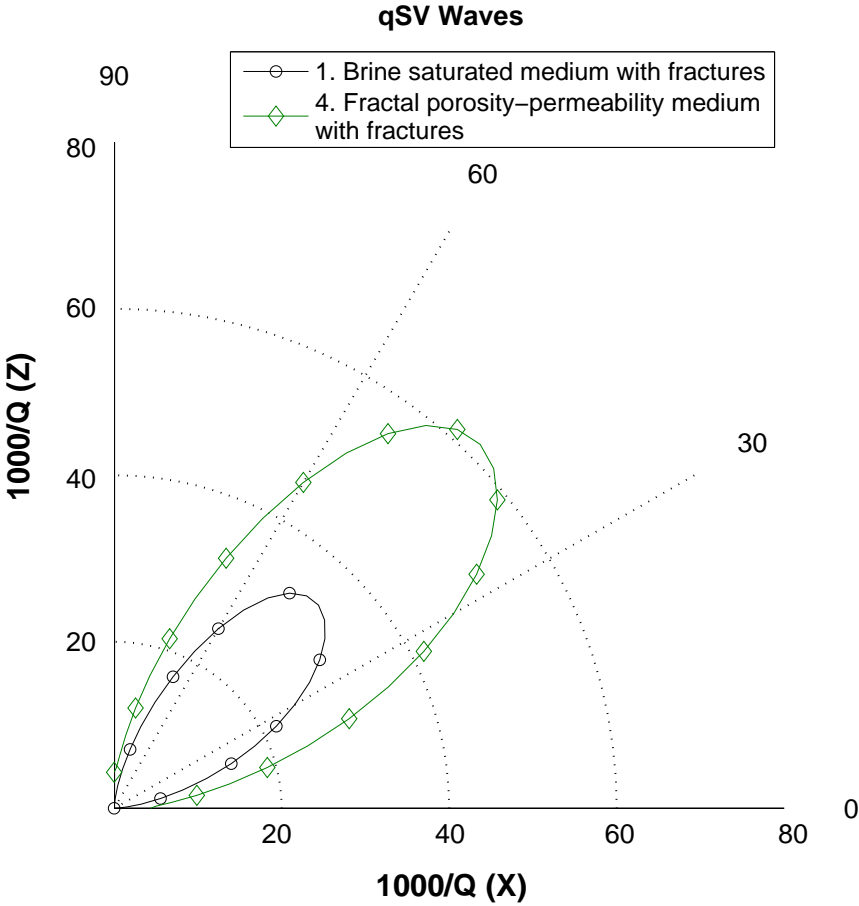
Note the increase in Q anisotropy for angles between 30 and 60 degrees

The model: Ω **consists of an anisotropic rotated TIV layer between two isotropic half-spaces.**

The upper half space has P- and S-wave velocities equal to 1890 m/s and 592 m/s, respectively, while the lower half-space has P- and S-wave velocities of 2320 m/s and 730 m/s.

The anisotropic layer, with a thickness of 300 m, is an viscoelastic medium with five complex and frequency dependent stiffness obtained using the upscaling procedure. The medium is rotated by 20 degrees , i.e., the angle between the symmetry axis and the vertical direction.

The average density in Ω **is 2300 kg/m3.**

The mesh consists of square cells having side length 3.7 m.

The source is a dilatational perturbation of central frequency is 30 Hz, located 150 m below the first interface (an asterisk in the figures).
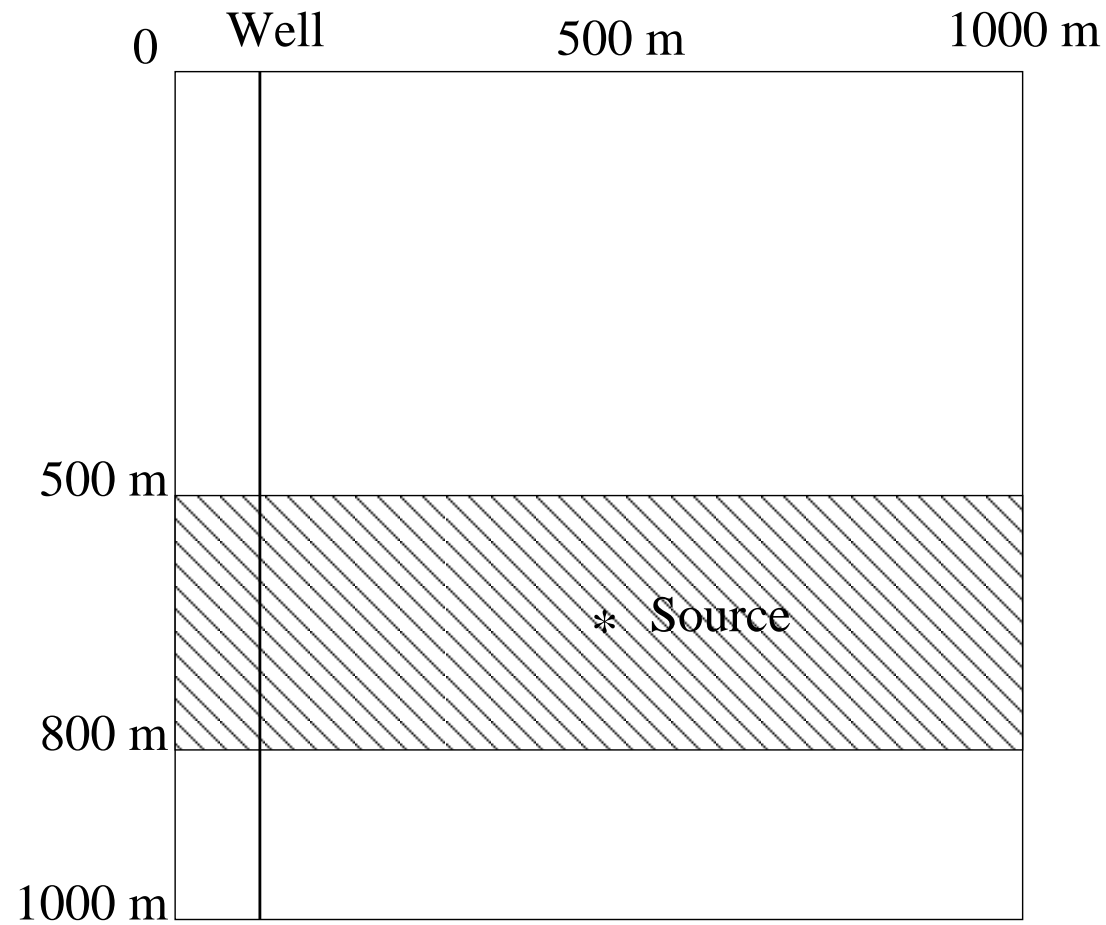
The Macroscopic TIV model.

The Macroscale. III. Seismic modeling.

We solve the following boundary value problem at the macroscale (in Ω):

$$-\omega^2 \rho u - \nabla \cdot \tau(u) = F, \quad \Omega$$

$$-\tau(u)\nu = i\omega \mathcal{D}u, \quad \partial\Omega, \text{(absorbing bounday condition, } D > 0\text{)}$$

$u = (u_x, u_z)$**: displacement vector,** ρ**: average density.**

$\tau(u)$**: stress-tensor of our equivalent viscoelastic material, defined in terms of the** $p'_{IJ}s$**.**

Instead of solving the global problem associated with the above model, we obtained the solution using a parallel FE iterative hybridized domain decomposition procedure employing a nonconforming FE space.

A run in santalo under MPI with 100 processors required 10 hours of CPU time for 1000x1000 mesh, 6.000.000 unknowns and 900 frequencies.
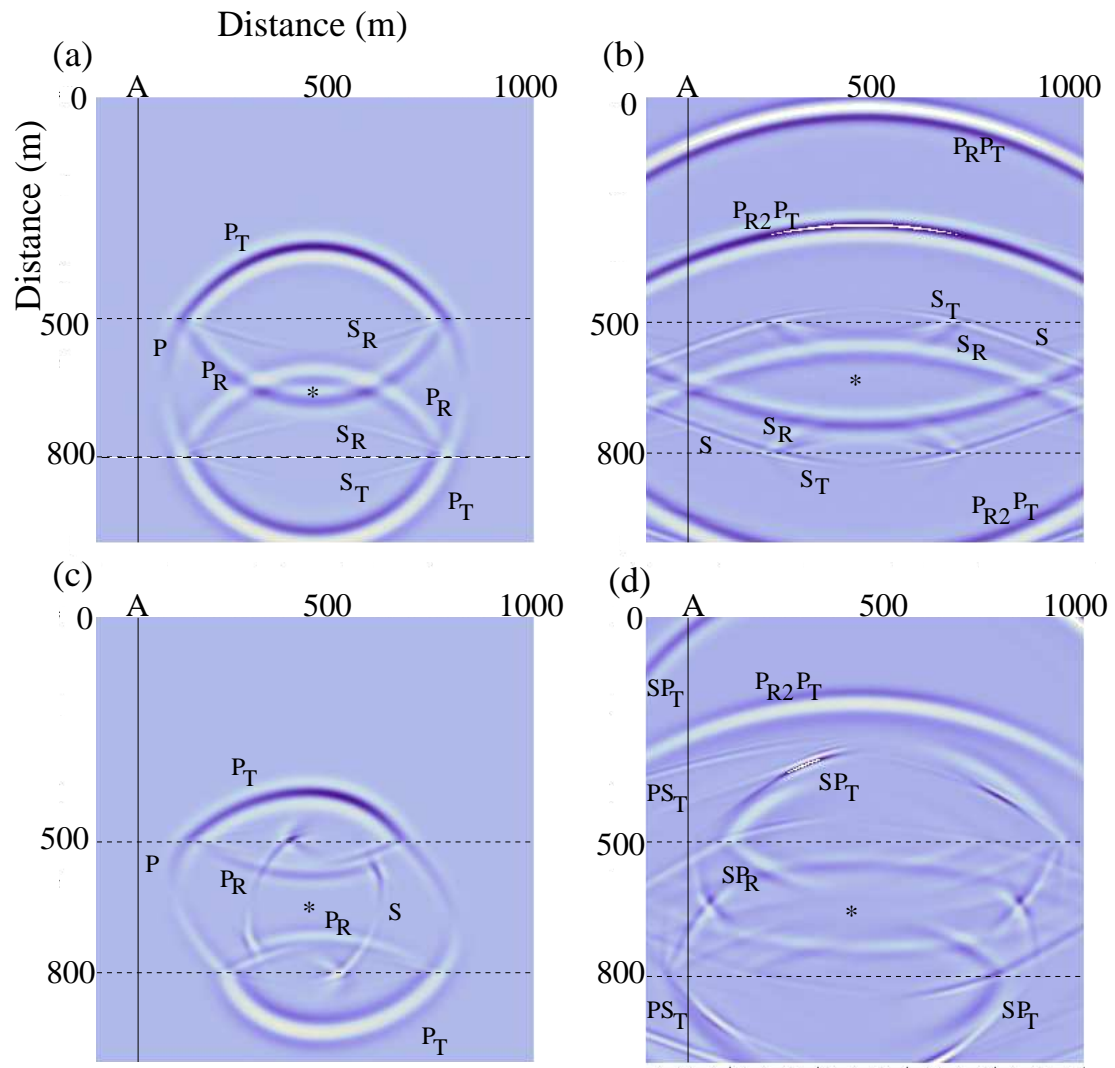
Ideal isotropic case (left, a and b) and real (rotated TIV) case (right, c and d).

- Storage of CO_2 in geological formations is a procedure employed to reduce the amount of greenhouse gases in the atmosphere to slow down global warming.

- Geologic sequestration involves injecting CO_2 into a target geologic formation at depths typically >1000 m where pressure and temperature are above the critical point for CO_2 (31.6C, 7.38 MPa).

- Example of injection into the Utsira Sand, a saline aquifer at the Sleipner field, North Sea.

- Time-lapse seismic surveys aim to monitor the migration and dispersal of the CO_2 plume after injection.
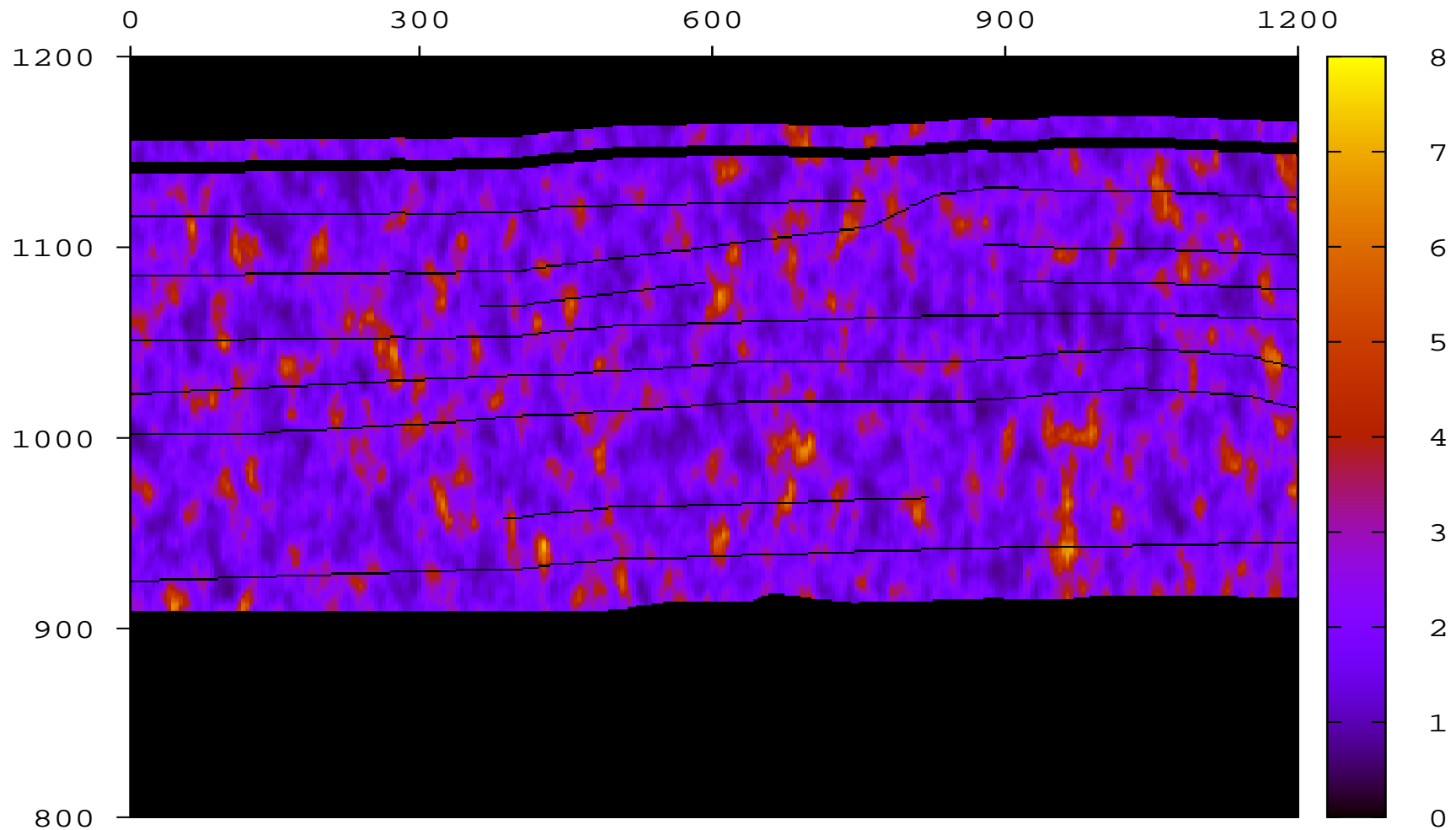
The thin lines represent mudstone layers within the formation.
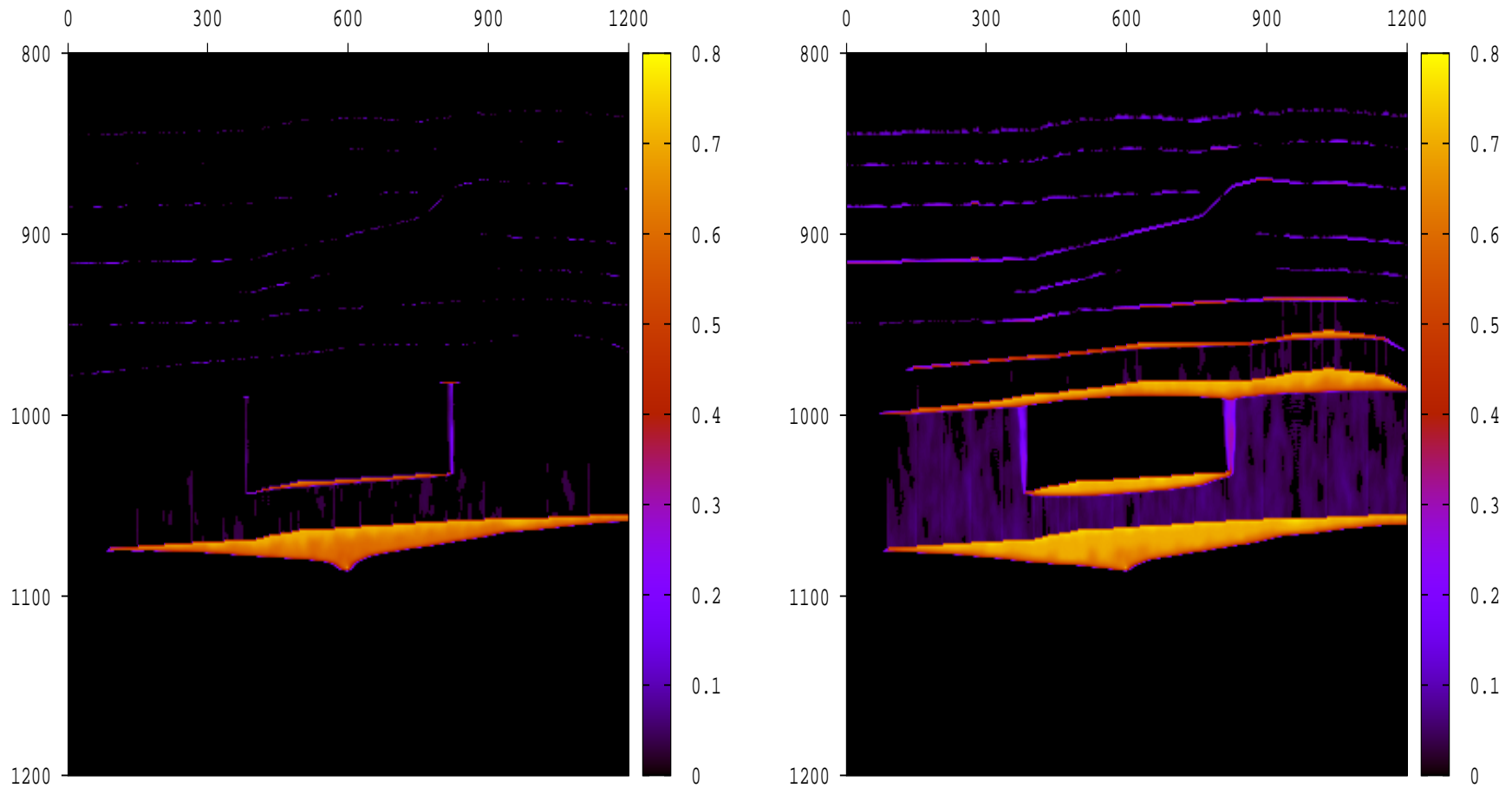
CO$_2$ saturation distribution after 2 years (left) and 6 years(right) of CO$_2$ injection

Observe a decrease in P- wave velocity (left) and a decrease in attenuation coefficient Q_p (right) in zones of CO_2 accumulation. Mesoscopic attenuation adn dispersion effects are taking into account using a White model.
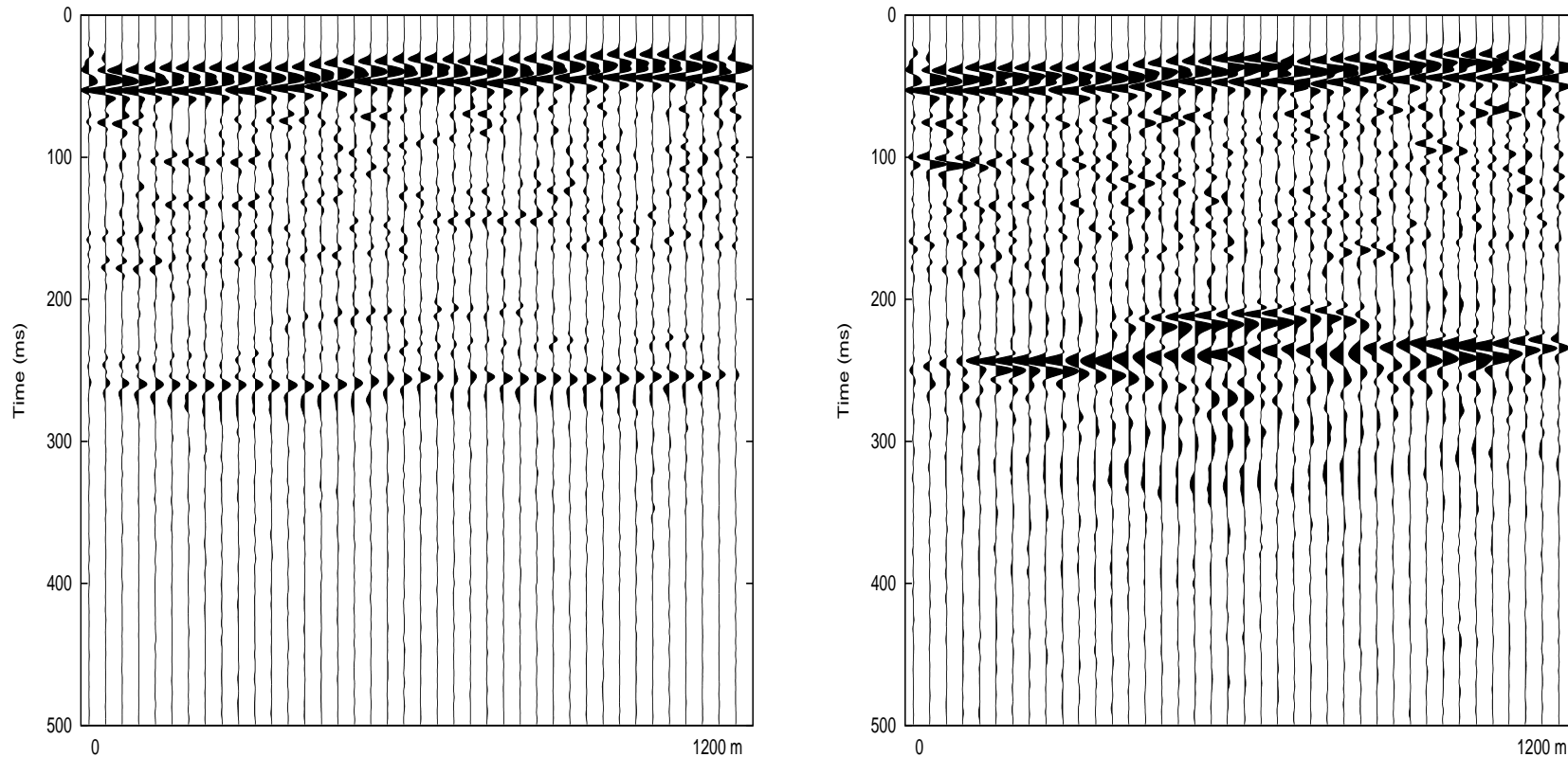
Traces of the z-component of the particle velocity before (left) and after 2 years (right) CO_2 injection. The two arrivals seen on the left Figure come from the base and top of the Utsira. The strong later arrivals seen on the right Figure are due to P-waves reflected at CO_2 accumulations and the base of the Utsira.
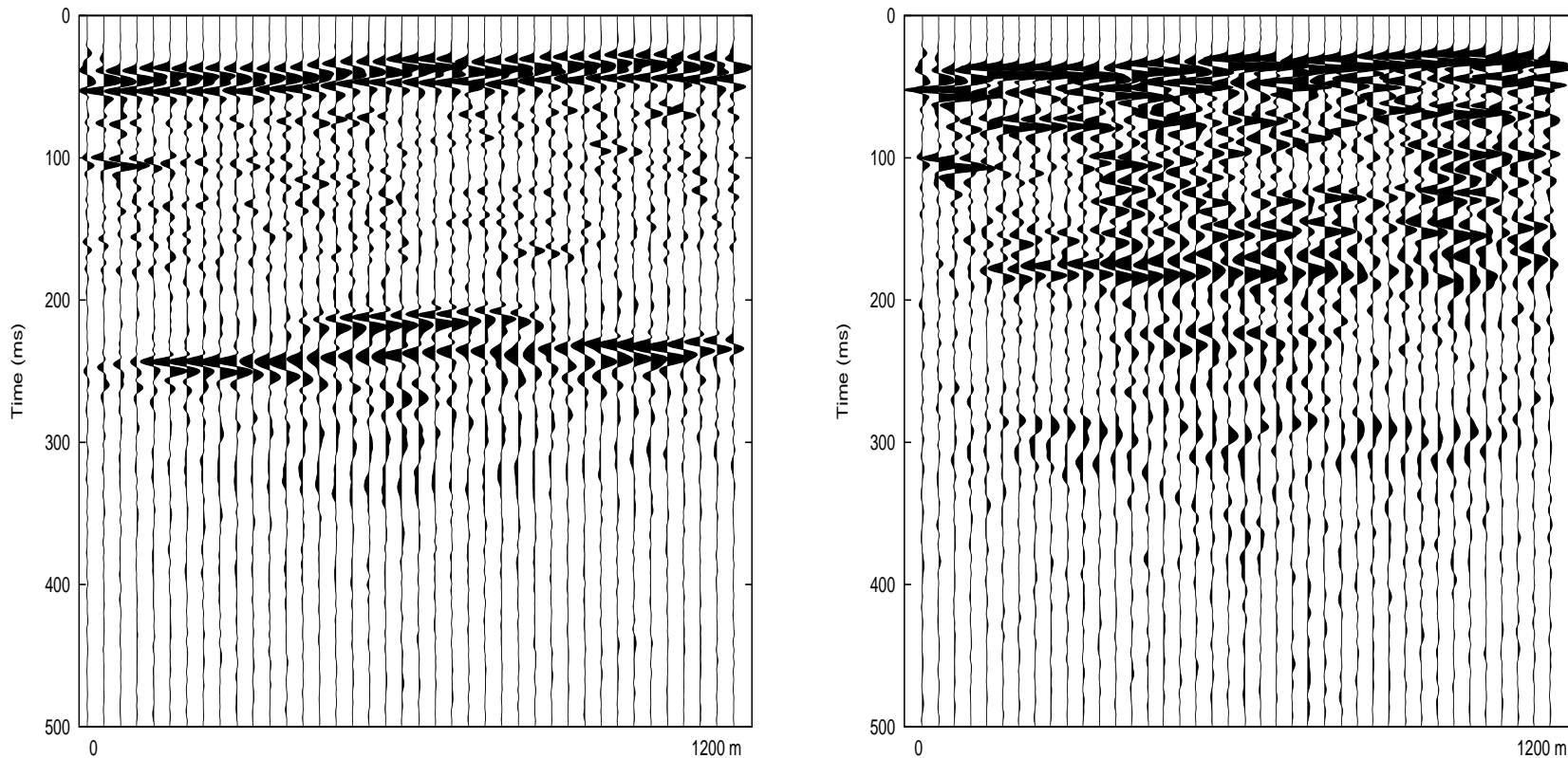
Traces of the z-component of the particle velocity after 2 years (left) and 6 years (right) of CO_2 injection. The earlier arrivals on the right Figure are due to waves reflected at the CO_2 accumulations below the shallow mudstone layers.

Conclusions

- **Numerical upscaling procedures allow to represent mesoscopic scale heterogeneities in the solid frame and saturant fluids, fractures and craks affecting observations at the macroscale.**

- **THE FEM is a useful tool to solve local problems in the context of Numerical Rock Physics and global problems at the macroscale.**

- **The techniques presented here to model acoustics of porous media can be extended to other fields, like ultrasound testing of quality of foods, groundwater flow and contamination among others.**

- **Thanks for your attention !!!!!.**